CrossMark

Preparation and photocatalytic performance of fibrous Tb^{3+}-doped TiO_2 using collagen fiber as template

Ting Luo[1] · Xiang-Jun Wan[1] · Shang-Xuan Jiang[1] · Li-Yuan Zhang[1,2] · Zheng-Qu Hong[1] · Jiao Liu[1]

Abstract

Fibrous Tb^{3+}-doped TiO_2 were prepared using collagen fiber as template. Morphology, crystalline structure, surface area, element content, chemical composition and elemental chemical status, microstructure and element distribution of the prepared samples were characterized by using scanning electron microscopy, X-ray diffraction, specific surface area analysis, inductively coupled plasma atomic emission spectrometer, X-ray photoelectron spectroscopy, transmission electron microscope and element mapping, respectively. The photocatalytic activities were evaluated by following degradation of methyl orange. The results showed that the fiber structure of collagen template was fully preserved when the calcination temperature was 500–800 °C. However, with the increase of calcination temperature, crystallinity and average particle size were increased, and the photocatalytic performance was decreased. For 2% Tb^{3+}–TiO_2 calcined at 500 °C, the degradation rate of methyl orange reached 93.87% after 6 h when a high-pressure mercury lamp (150 W) was used as the light source for photocatalytic degradation. Titanium tanning agent performance was excellent, the yield of TiO_2 was high, and the fiber structure was presented when 0.2 mol/L citric acid/sodium citrate buffer solution was used.

1 Introduction

Titanium dioxide, an n-type semiconductor material, is widely applied to photocatalytic materials due to its low cost, nontoxicity and strong oxidizing power [1]. When TiO_2 is at nanometer size, it has broad applications in the fields of ceramics, coatings, cosmetics, industrial catalysts, environmental protection, etc., [2–6] because of its large specific surface area and enriched surface active sites. This material plays an especially important role in the degradation of organic pollutants [7] due to its unique physical and chemical properties. However, low photoconversion due to the rapid electron–hole recombination leads to the difficulty for TiO_2 to be a practical catalytic agent [8]. Moreover, TiO_2 only absorbs UV light with wavelengths less than 380 nm because of its wide band gap (3.2 eV), and its utilization efficiency of solar light is below 5% [9]. Consequently, its

practical applications in photocatalysis are seriously hindered. To improve its photocatalytic activity, the preparation and modification of nanometer-sized titanium dioxide (nano-TiO_2) have become a hot topic in recent decades. To date, the preparation methods of nano-TiO_2 can be classified into physical methods, chemical methods and comprehensive methods. The physical methods include vacuum evaporation [10], sputtering [11], mechanical crushing [12], and inert gas condensation [13]. The chemical methods involve electrochemical deposition [14] and ion implantation [15]. The physical and chemical comprehensive synthesis methods include sol–gel [16], hydrothermal synthesis [17], water-in-oil microemulsion [18], $TiCl_4$ gas phase process [19], and titanium alkoxide hydrolysis [20], and the synthesis of Si–Ti composite magnetic was also reported [21]. To modify titanium dioxide, precious metals, transition metals, rare earth metals, and non-metallic elements have been used to dope or co-dope titanium dioxide to inhibit the recombination of photogenerated electrons and holes and to improve the light utilization rate [22–28]. Previous studies have shown that doping with rare earth metal elements can form lattice defects on the surface of TiO_2, and shift the light absorption band to visible light [29]. In addition, rare earth metal elements are considered as effective doping agents to improve the photocatalytic performance of TiO_2.

✉ Li-Yuan Zhang
  zhangliyuansir@126.com

[1] College of Chemistry and Chemical Engineering, Neijiang Normal University, Neijiang 641112, China

[2] Key Laboratory of Fruit Waste Treatment and Resource Recycling of the Sichuan Provincial College, Neijiang 641112, China

The photocatalytic properties of TiO_2 are affected by the crystal morphology, phase, size and specific surface area. It has been reported that the mesoporous TiO_2 has a large specific surface area, and can provide more active sites [30, 31] for the photocatalytic reaction than the bulk crystalline TiO_2. Thus, the mesoporous structure can effectively improve the photocatalytic performance. So far, the template method [32] is the most commonly used to prepare TiO_2 with a specific morphology. A predictable structure and performance of the product can be obtained by using a template with a certain structure. Therefore, the choice of template plays a dominant role in the structure and properties of the target material.

Collagen is one of the most abundant biomass resources in the world, which is mainly used in leather processing. However, the utilization rate is so low that a large amount of skin collagen is often treated as solid waste. The fiber structure of skin collagen dispersed and lost because it is composed of spiral-shaped structures formed by three-peptide chains. Coarse fiber bundles are woven by a large numbers of fine fibers, which are arranged in a special criss-cross pattern forming a three-dimensional network [33]. In addition, collagen contains –OH, –COOH, –NH_2 and other functional groups which can effectively coordinate with metal ions [34]. Thus, skin collagen fiber is an ideal template to prepare materials with fibrous structure. Furthermore, using the skin collagen fiber as the template for the synthesis of functional materials could be a potential way to recycle solid waste produced in leather processing industry.

The present study aimed at testing the feasibility of doping TiO_2 with rare earth to effectively increase the photocatalytic performance of titanium dioxide due to improved electronic structure, optical properties [35] and capable of textile dye degradation [22]. So far, among all of rare earth elements used for doping, La has been studied most frequently, followed by Ce, Er, Pr, Gd, Nd, Sm, Ho, etc., while research on increasing photocatalytic performance by doping with terbium is rarely reported. It can be seen from the electron configuration of terbium that it has a 4f shell that is partially filled and a 4f electron spin orbit coupling. In addition, electron energy of 4f, 5d and 6s is similar. So, it has the capacity to produce more energy levels, and thus it is easy to form the doping energy levels which contribute to improve photon utilization via arousing the captured electron on the doping ion with the low energy photon. Furthermore, terbium is a rare earth element with variable valence and can lead to redox reaction on the surface of titanium dioxide which will produce vacancy oxygen (V–O) to improve the photocatalytic activity [36], therefore, it is necessary to test the application of terbium as the doping source.

In this work, fibrous Tb^{3+}–TiO_2 were synthesized by employing titanium sulfate as the titanium source, and terbium nitrate as the doping source in aqueous solution. A mesoporous structure was obtained by removing the collagen fiber template via calcination, and the photocatalytic performance of the product was evaluated by following the degradation of methyl orange.

2 Experimental

2.1 Preparation of catalyst

2.4 g $Ti(SO_4)_2$ was added into a 250-mL beaker, followed by 35 mL citric acid/sodium citrate buffer solution, Then pH of the solution was adjusted to 2.0 using saturated sodium bicarbonate solution to get the stock solution. After 1.5 g hide powders were added into a 250 mL beaker, 0.6 g NaCl and 25 mL distilled water was added, and the pH value of the solution was adjusted to 2.0 with the mixed solution of sulfuric acid (25 wt%) and formic acid (in mass concentration ratio 3:1). Subsequently, this solution was stirred at room temperature for 4 h, and then the stock solution was added. After a reaction for 8 h, the pH of the solution was adjusted to 4.0 with saturated sodium bicarbonate solution and the system was kept at 38 °C while stirring for 2 h. Then the system was centrifuged and washed with distilled water. The obtained collagen was added into terbium nitrate solution and stirred for reaction for 2 h. Then the resulted materials were washed with deionized water, and soaked with alcohol. After being dried naturally in air, the obtained powders were calcined at different temperatures to get the TiO_2 doped with Tb^{3+} (Tb^{3+}–TiO_2).

2.2 Evaluation of photocatalytic performance

0.05 g Tb^{3+}–TiO_2 powders with different doping dosages of Tb^{3+} were added into 25 mL aqueous solution of methyl orange (20 mg/L). The mixture was kept in dark conditions while being stirred using a magnetic bar for 30 min to avoid the influence of adsorption of methyl orange by TiO_2. After that, a high-power mercury lamp (150 W with a main wavelength of 365 nm) was turned on to start the photocatalytic experiment.

After the photocatalytic degradation experiment, the solution was taken and placed in a quartz cuvette, and the absorbance value at 465.5 nm was recorded using a UV–Vis spectrometer. The results were processed according to the following equation:

$$X = (A_0 - A_t)/A_0 \times 100\%, \tag{1}$$

where A_0 is the initial absorbance, A_t presents the absorbance of the solution at time t, and X is the decolorization rate at time t.

2.3 Characterization

The microscopic structures of the samples were characterized by scanning electronic microscopy (SEM, VEGA3, TESCAN, Czech Republic). The crystalline structure of the samples was investigated with X-ray diffractometer (XRD, DX-2700, Dangdong Haoyuan Instrument Co., Ltd., China) using Cu Kα radiation at a scanning rate of 0.05° s^{-1} and a working voltage/current of 40 kV/40 mA. The photocatalytic performance was evaluated using a photochemical reactor (BL-GHX-V, Shanghai Bilon Instruments Co., Ltd., China). The absorbance of methyl orange was collected by a UV–visible spectrophotometer (Model 752, Shanghai Xin Mao Instrument Co., Ltd., China). The pore size and specific surface area were described by a surface area analyzer (BET, Autosorb iQ2, Quantachrome, USA). The titanium ion concentration was analyzed by inductively coupled plasma atomic emission spectrometer (ICP-AES, IRIS Advantage, Thermo Fisher Scientific, USA). The chemical composition and elemental chemical status were investigated by X-ray photoelectron spectroscopy (XPS, Escalab 250 Xi, Thermo Fisher Scientific, USA). The microscopic structures of the samples were also characterized by transmission electron microscope (TEM, JEM 2010, Japan Electron Optics Laboratory Co., Ltd., Japan). The element distributions of samples were tested by element mapping using a field emission scanning electron microscope (FESEM-EDS, Sigma 300, Carl Zeiss Co., Ltd., Germany).

3 Results and discussion

3.1 Crystalline structure

Based on the XRD spectra of undoped TiO$_2$ prepared using collagen as the template and calcined for 4 h at 500, 600, 700 and 800 °C (Fig. 1), it is evident that the samples are mainly composed of anatase phase while TiO$_2$ calcined at 700 and 800 °C also contain a small portion of rutile phase. It is also shown that the degree of crystallinity of the samples increases with the elevation of calcination temperature. It can be seen from Fig. 2 that the degree of crystallinity of TiO$_2$ decreases obviously after being doped with 2% terbium nitrate and calcined at 600 °C (Fig. 2). The average grain sizes of TiO$_2$ and Tb^{3+}–TiO$_2$ powder samples were calculated using the Scherrer formula, and the results are given in Table 1. The results show that the average grain size of TiO$_2$ calcined at 500 °C is 16.1 nm while the value of TiO$_2$ doped with 2% terbium nitrate is 9.6 nm, illustrating the inhibition effect of a small portion of Tb^{3+} on the growth of TiO$_2$ grains. Since the radius of Tb^{3+} (92 pm) is greater than that of Ti^{4+} (68 pm), it is easy to for Ti^{3+} to form substitutional solid solution and produce Ti–O–Tb bond rather
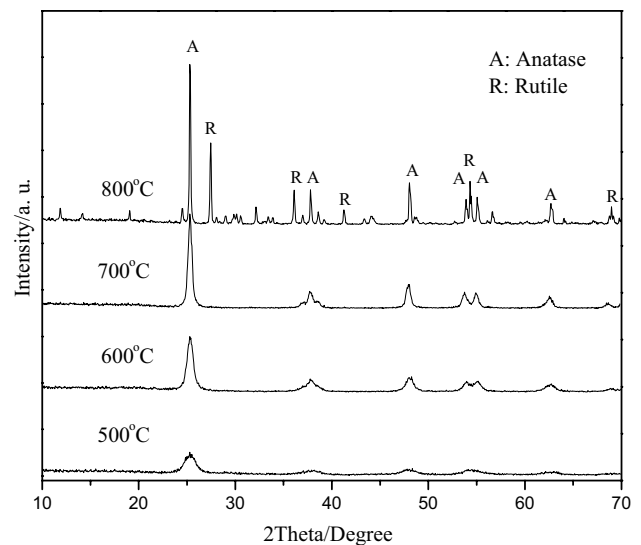

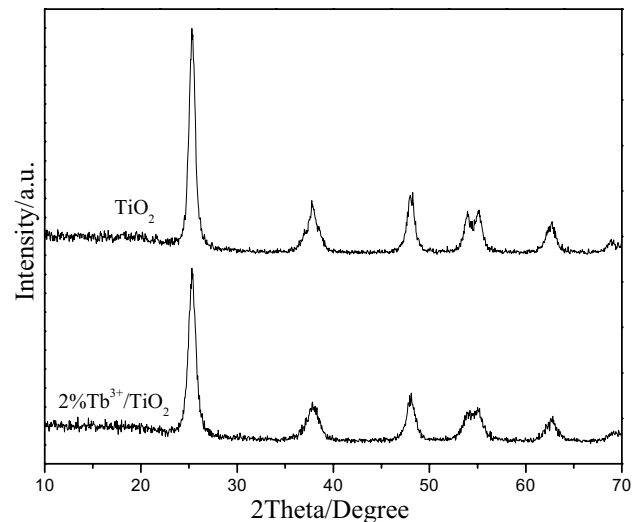**Fig. 1** XRD patterns of undoped TiO$_2$ calcined at 500–800 °C

Fig. 2 XRD patterns of 2% Tb^{3+}–TiO$_2$ calcined at 600 °C

than interstitial solid solution, then the doping atoms migrate to the surface of crystal or the inner surface of the normal position of the node, leading to elastic distortion around the lattice. This process leads to the deviation of the original complete structure, and leaves vacant in the crystal. As a result, the growth of TiO$_2$ grains is inhibited because of the lattice defection with the microstress.

In addition, the crystal phase composition can be calculated according to Eq. (2), and the results are shown in Table 2.

$$X_A = 100/[1 + 1.265(I_R/I_A)], \tag{2}$$

Table 1 Grain sizes of TiO_2 and Tb^{3+}–TiO_2

CPI (hkl)	TiO_2, size (nm)				2% Tb^{3+}–TiO_2, size (nm)			
Temperature (°C)	500	600	700	800	500	600	700	800
Anatase TiO_2								
(101)	7.6	11.9	15.0	60.1	6.9	9.5	14.1	18.1
(004)	17.2	20.7	19.3	54.3	15.0	11.3	21.7	27.3
(200)	13.9	10.0	14.6	44.8	7.9	20.9	15.7	17.7
(105)	24.6	25.0	17.7	82.4	9.0	14.3	22.9	21.7
(211)	17.0	16.7	19.0	68.7	9.0	9.2	20.3	17.3
Average	16.1	16.9	17.1	62.1	9.6	13.0	18.9	20.4
Rutile TiO_2								
(110)	–	–	124.4	60.4	–	–	–	50.5
(101)	–	–	102.0	58.6	–	–	–	44.4
(211)	–	–	57.3	82.5	–	–	–	38.1
Average	–	–	94.6	67.2	–	–	–	44.3

Table 2 Contents of anatase in TiO_2 and Tb^{3+}–TiO_2

Temperature (°C)	500	600	700	800
TiO_2/%	100	100	97.96	62.48
2% Tb^{3+}/TiO_2/%	100	100	100	97.79

where I_A and I_R are the intensity of the characteristic diffraction peak of anatase phase (101) and the rutile phase (110), respectively.

The results indicate that rutile phase exists in undoped TiO_2 calcined at 700 °C, while signs of rutile phase cannot be detected in TiO_2 doped with Tb^{3+} until a calcination at 800 °C. It can be concluded that the doping of Tb^{3+} has a certain inhibitory effect on the phase transition of TiO_2.

3.2 Morphology characterization

SEM images of 2% Tb^{3+}–TiO_2 calcined at 500, 600, 700 and 800 °C for 4 h are given in Fig. 3. It is clear that the Tb^{3+}–TiO_2 has a fiber structure, and the outer diameter of the fiber bundle is approximately 2 μm, similar to that of the natural collagen fiber bundle. Moreover, each fiber bundle is arranged relatively loosely, suggesting that the Tb^{3+}–TiO_2 prepared using collagen template retains the original mesoporous fiber structure completely. In addition, comparing the four images in Fig. 3, the fiber structure is looser in Fig. 3a and the fiber structure is more obvious at 500 °C. However, with the increase of temperature, the distance between fiber bundles decreases gradually. These results suggest that the capability of Tb^{3+}–TiO_2 to maintain the original fiber structure of the collagen template decreases with the increment of temperature, which is in agreement with the result that the photocatalytic property of Tb^{3+}–TiO_2 materials obtained at 500 °C is the best which will be discussed later.

## 3.3 Effect of Tb^{3+} doping on the performance of TiO_2

The outer electron orbit of Tb^{3+} ion used in this work is $4f^9 6s^2$, and 4f electronics are not introduced between the top of the valence band and the bottom of the conduction band. Tb_{4f} and Tb_{5d} have little influence on the bandgap, and they participate in the composition of the top of the valence band and the bottom of conduction band [37]. However, as discussed above, the doping of Tb^{3+} can hinder the growth of TiO_2 grains. Thus, the specific surface area increases and more reactive sites are available, resulting in a more complete reaction. Therefore, the appropriate amount of Tb^{3+} doping helps to improve the photocatalytic performance of TiO_2.

In addition, an appropriate terbium doping activates a part of interior electrons to escape from TiO_2, leading to the separation of electron–hole and the inhibition effect is efficient for the lattice defection. The activated electrons get rid of the nucleus restraint becoming the carrier, and the special electronic layout structure of terbium itself has the capacity to generate the shallow energy level to capture carrier and hole trap. The shallow energy level not only makes the band gap of TiO_2 decrease, but also makes it easier for the shallow level of electron to migrate to surface, and participates in photocatalytic reaction, resulting in an improved photocatalytic activity because of the higher energy [38].

Under normal circumstances, the temperature at which pure anatase TiO_2 transforms into rutile is 610–915 °C [39]. As shown in Fig. 4, undoped titanium dioxide prepared by calcination at 600 °C for 4 h using collagen template has the highest photocatalytic property, and its crystal phase is completely anatase. Its degree of crystallinity is better as suggested by the obvious characteristic peak of anatase phase; thus, the photocatalytic performance is improved [40] as compared with the particles calcined at 500 °C.
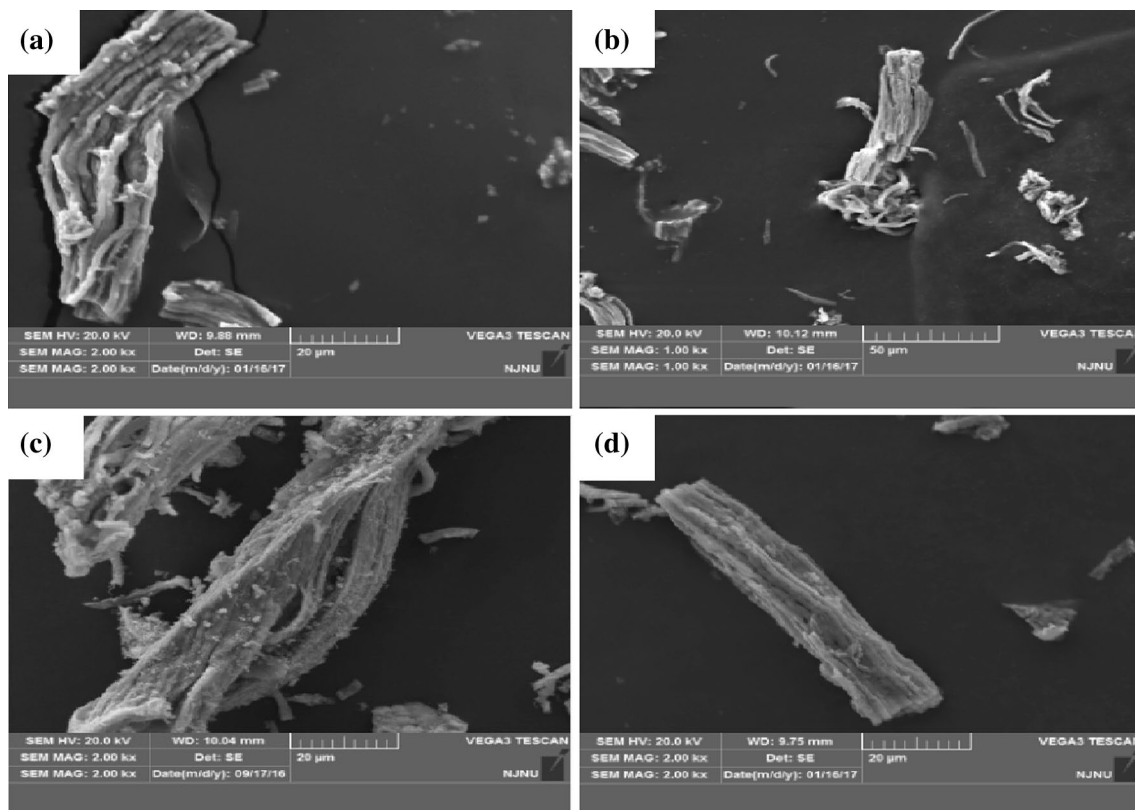
Fig. 3 SEM images of 2% Tb^{3+}–TiO_2 calcined at different temperatures. **a** 500 °C, **b** 600 °C, **c** 700 °C, and **d** 800 °C
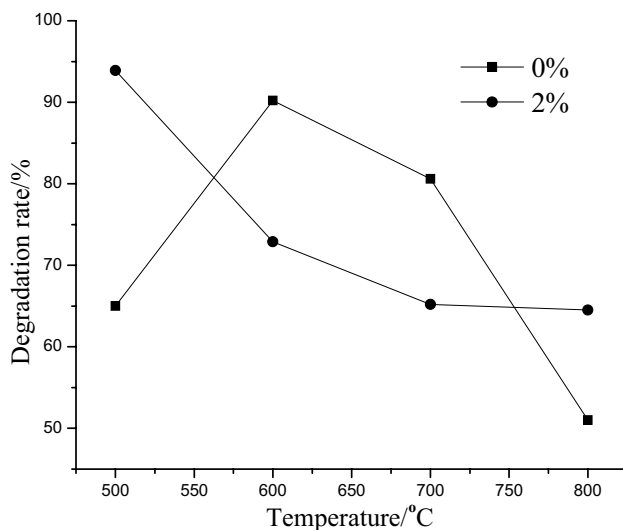
Fig. 4 Degradation rates of methyl orange by TiO_2 and Tb^{3+}–TiO_2 obtained by calcination at different temperatures

The photocatalytic activity of the undoped TiO_2 calcined at 700 °C was obviously reduced, suggesting that the phase transition temperature is between 600 and 700 °C, which is in good accordance with the results listed in Table 2. The results given in Table 2 also shows that the phase transition temperature of Tb^{3+}–TiO_2 is 700–800 °C, indicating that the doping of Tb^{3+} can inhibit the phase transition of TiO_2, which is consistent with the work of Zhang et al. [41]. The doping of metal ions can cause the change of the particle size of TiO_2. For example, Sm doping can form Sm–O–Ti and hinder the growth of TiO_2 crystal [42]. It was also reported that Ce and La doping can inhibit the growth of titanium dioxide particles, and the grain growth rate was also slowed down [43]. The smaller the grain size, the more the phase transition can be inhibited [41]. In this work, the crystal growth is hindered and the grains decrease due to the doping of rare earth element Tb^{3+}. As a result, the phase transition temperature is increased. However, Fig. 4 also shows that the photocatalytic performance of Tb^{3+}–TiO_2 catalyst calcined at 600–800 °C is not as good as that of the catalyst calcined at 500 °C. The reason is that, although the doping of Tb^{3+} can inhibit the growth of crystal grains and reduce the average grain size. However, the Tb^{3+}–TiO_2 obtained at 600–800 °C is still much larger than that at 500 °C (Table 1). As shown in Table 3, when the doping ratio is 2%, the specific surface area of the catalyst calcined at 500 °C is much higher than that at 600 °C under the same conditions. In other words, the contact area of the materials in the reaction at a higher calcination temperature is obviously reduced,

Table 3 Pore size and specific surface of the samples

| Sample	Pore size (nm)	Specific surface
500 °C 0%Tb^{3+}	6.006	52.731
500 °C 2% Tb^{3+}	5.298	56.449
600 °C 0%Tb^{3+}	5.816	29.498

and the reaction may be incomplete. Therefore, although the anatase phase still exists in the samples calcined at 600–800 °C, the photocatalytic activity of Tb^{3+}–TiO$_2$ is not as good as that of Tb^{3+}–TiO$_2$ calcined at 500 °C.

As shown in Fig. 4, the photocatalytic performance of Tb^{3+}–TiO$_2$ is not as good as that of undoped TiO$_2$ calcined at 600–700 °C, which can be explained by the data in Table 1. When calcined at 600–700 °C, the average grain size of Tb^{3+}–TiO$_2$ and TiO$_2$ have little difference. However, the size of Tb^{3+} is much larger than that of Ti^{4+}, and a part of contact area will be occupied during the catalytic reaction. As a result, the effective contact surface area is reduced. Thus, Tb^{3+}–TiO$_2$ calcined at 600–700 °C has a better photocatalytic performance than the undoped TiO$_2$ calcined at the same temperature range. It is worth mentioning that the average grain size of Tb^{3+}–TiO$_2$ is much smaller than that of undoped TiO$_2$ calcined at 800 °C, which also contributes to a better photocatalytic performance.

3.4 Effect of doping dosage on photocatalytic performance

It has been reported in previous work that the thickness of the surface charged layer of doped TiO$_2$ can be used as a parameter for evaluating the optimum doping amount of metal ions. The photogenerated electrons and holes can be separated most effectively when the surface thickness is equal to the incident depth, and the highest [44] light utilization can be achieved at this point. Thus, almost all the metal elements used to dope TiO$_2$ have an optimum doping amount. Figure 5 shows the degradation rates of methyl orange by Tb^{3+}–TiO$_2$ with different doping amounts calcined at 500 °C for 4 h. It is shown that the photocatalytic performance of Tb^{3+}–TiO$_2$ is the best when the doping ratio is 2%. The photocatalytic activity of TiO$_2$ can be improved by the doping dosage used in this work. After analysis of the property of Tb^{3+}, it can be seen that the lattice structure of TiO$_2$ was affected after doping which forms lattice defection, produces shallow energy level to capture carrier and hole trap, reduces the width of band gap and inhibits the combination of electron and hole. Thus, the photocatalytic performance of Tb^{3+}-doped TiO$_2$ is improved.

However, doping TiO$_2$ with Tb^{3+} above a certain level might lead to decreased photocatalytic performance. Tb^{3+} replaces Ti^{4+} on the crystal surface or the inner surface of
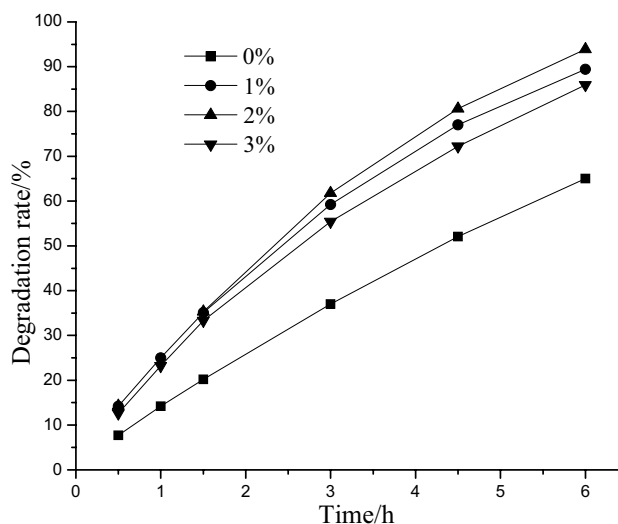

Fig. 5 Degradation rates of methyl orange by Tb^{3+}–TiO$_2$ with different doping amounts calcined at 500 °C for 4 h

the normal position by substitution method. On one hand, the doping of terbium makes lattice distort, which increases the reaction activity and improves the photocatalytic performance; on the other hand, the atomic radius difference is more than 15% which limits solubility in TiO$_2$ and cannot form infinite solid solution. When the doping amount of terbium exceeds a certain value, it will cause lattice instability owing to a high energy, and a part of terbium accumulates on the surface of lattice. At the same time, the crystal with a higher energy tends to adsorb other heteroatoms on the surface so as to reach a stable state. In addition, the radius of Tb^{3+} is much larger than Ti^{4+}, and it can reduce the effective contact surface and the area of mesoporous which is enable to restrain the recombination of electron–hole when Tb^{3+} is excessive. Thus, the sites for the photocatalytic reaction are reduced which results in the decreased photocatalytic performance [8]. Furthermore, although the excessive Tb^{3+} cannot exchange with Ti^{4+} in the crystal lattice, it can stay on the surface of TiO$_2$ when the doping dosage is beyond a certain content (2% in the present study). The excessive Tb^{3+} would rather play the role of recombination center than facilitate electron–hole separation [45, 46], which leads to the decreased photocatalytic activity.

3.5 XPS analysis

To analyze the chemical composition and states, XPS characterization was carried out, shown in Fig. 6. It can be seen from Fig. 6 that the samples are mainly composed of Ti, O, in addition, a few of carbon is observed, which is derived from exogenous pollutants [47]. As can be seen in Fig. 6a, the full spectrum indicates that the proportion of titanium and oxygen before doping is 1:1.998 and that of after doping
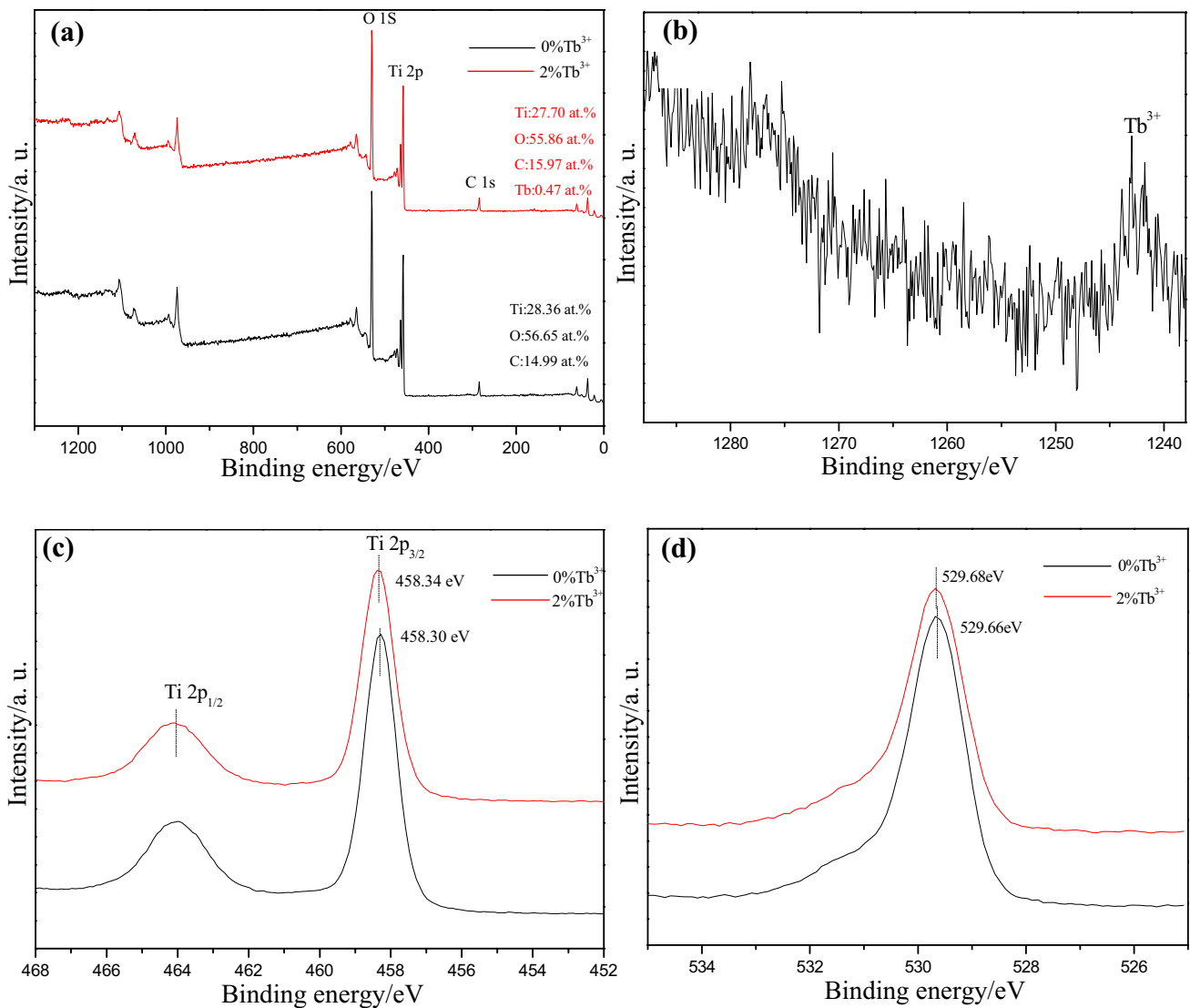
Fig. 6 XPS patterns of pure TiO$_2$ and 2% Tb^{3+}–TiO$_2$ calcined at 500 °C for 4 h. **a** Full spectrum; **b** characteristic absorption band of terbium; **c** high-resolution XPS spectra of the Ti$_{2p}$ core levels; **d** high-resolution XPS spectra of the O$_{1s}$ core levels

is 1:2.017. It suggests that the oxygen content is increased slightly after the terbium doping. It is because the XPS mainly measures the elemental composition of lattice surface. After doping, there are some terbium ions distributed on the surface of TiO$_2$. Due to the strong chemical activity they own, a strong binding ability could be formed between Tb^{3+} and O, which results in a larger oxygen content on the surface [48]. Figure 6c shows the Ti$_{2p}$ spectra with a doublet, whose binding energies are 458.30 and 464.01 eV that reflect Ti$_{2p3/2}$ and Ti$_{2p1/2}$ lines, respectively. The difference in value of binding energies indicates that Ti atoms exist in Ti^{4+} oxidation states [49]. In contrast, the peak of Tb^{3+}-doped TiO$_2$ shifts to a higher binding energy by 0.04 eV, and the peaks are clearly asymmetrical as shown in the 2P$_{3/2}$ peaks at the lower energy side which certifies the existence of Ti^{3+} [50].

The shift of Ti$_{2p3/2}$ peak toward to higher binding energy is related to Tb doping, which leads to the change of electron cloud around Ti atom, and the increase of Ti$_{2p3/2}$ and Ti$_{2p1/2}$ binding energy. In addition, the existence of Ti^{3+} can effectively restrain the recombination of photoelectrons and holes, and improve photocatalytic activity [50].

The situation of O$_{1s}$ is shown in Fig. 6d. The orbit component of O$_{1s}$ for Tb^{3+}–TiO$_2$ binding energy is 529.68 eV, which shifts to a higher binding energy by 0.02 eV in comparison with pure TiO$_2$. It means the rise of Ti–O bond energy owing to oxygen vacancy defect which caused by Tb doping. The high-resolution scans of Tb are shown in Fig. 6b. For the Tb^{3+}-doped TiO$_2$, Tb absorption band appears at 1242.97 eV, which confirms the existence of terbium on the TiO$_2$ surface. Besides, as shown in Fig. 6a that

the proportion of terbium is 0.47 at.% (3.2 wt%), which is more than the original doping amount (2 wt%). It means that the terbium does not distribute in the lattice or interstitial sites evenly and a part of terbium stays on the TiO_2 surface that makes the high level concentration of terbium on the surface.

3.6 ICP-AES analysis

To analyze titanium content in the synthesized samples, ICP-AES analysis was used. The pre-treated processes of samples are given as follows: 20 mL concentrated sulfuric acid was added to 0.1 g TiO_2 and 0.1 g 2% Tb^{3+}–TiO_2, respectively, followed by heating with the electric furnace to dissolve the solids completely. After that, the liquid samples were diluted 1000 times, and then the concentration of Ti was determined by ICP-AES, shown in Table 4. It is known by XRD and XPS analysis, the anatase and rutile TiO_2 peaks in the patterns of XRD match the standard cards well without miscellaneous peak. It means that the sample which is mainly composed of Ti and O is in a high-purity level. In addition, as shown in XPS, the samples before and after Tb doping are mainly consist of Ti, O, and the proportion of Ti/O is close to 1:2, illustrating once again that the sample has a high-purity. As the result of ICP-AES shown in Table 4, the titanium content of undoped and 2% Tb^{3+}–TiO_2 are 59.78 and 60.56 wt%, respectively, which are close to the theoretical value (59.94 wt%). After Tb doping, the content of Ti is increased by 0.78 wt%, which also means the relative content of O is decreased. However, as mentioned above, the XPS results show that the ratio of Ti/O on the surface of samples before and after Tb doping are 1:1.998 and 1:2.017, respectively. In other words, XPS analysis illustrates that the content of O after Tb doping is increased. The reason for different conclusions is that the XPS mainly determines the element contents on the sample surface. After doping, the Tb on the sample surface has the ability to adsorb oxygen [48], which makes the slight increased of O content on the surface; however, the ICP-AES is used to test the content of Ti in the whole specimen. Due to the fact that Tb is trivalent while Ti is tetravalent, it will cause the decrease of positive charge in the crystal when a bit of Tb^{3+} replace Ti^{4+} forming substitutional solid solution. To keep charge balance, the crystal tends to generate oxygen vacancies to decrease

negative charge. As a result, after Tb doping, the content of O is decreased slightly in the whole sample.

3.7 TEM analysis

Figure 7a describes the microstructure of TiO_2 doped with 2% Tb^{3+} under the TEM characterization. A fibrous structure can be observed from Fig. 7a, which is consistent with the results of SEM. It illustrates once again that the fiber structure of the collagen template is completely maintained after the calcination. Besides, it can be seen that the diameter of fiber is approximately 50 nm with the length of micrometer scale. Figure 7b shows atomic arrangement of the undoped TiO_2. It can be seen that the arrangement of atoms presents multi-orientation, which means the crystal owns a polycrystalline structure. The crystalline interplanar spacing is measured to be 0.351 nm, which was marked in the figure, approximately equals to the theoretical value of anatase titanium dioxide (101).

Figure 7c, d shows the grain structure of undoped and 2% Tb^{3+}-doped TiO_2 at the same magnification. It can be observed that the grain size of undoped TiO_2 is 15–20 nm, while that of 2% Tb^{3+}–TiO_2 decreases to less than 10 nm. The values were coincident with the calculation results by Scherrer formula in Table 1. It can be concluded once again that terbium doping is able to restrain the growth of grain size.

3.8 Element mapping analysis

In order to further find out the element distribution of the specimens, element mapping was used to characterize the samples.

Figure 8a–d shows the images of the element distribution of 2% Tb^{3+}–TiO_2 and Fig. 8e–g gives the images of element distribution of the undoped sample. As can be seen from Fig. 8, Ti and O on the surface of samples before and after doping distribute evenly. Figure 8a, d shows that the terbium ions on the surface of sample distribute evenly and loosely without cluster.

3.9 Effect of titanium tanning agent

In addition to the above factors, the effect of titanium tanning agent was also considered in this work because it affects the tanning effect of titanium salt tannage in the leather craft. It has been reported that the tanning effect of titanium tanning is related to the preparation condition of bare skin and preparation methods, composition of the tanning agent, etc. Therefore, the concentration of citric acid and sodium citrate in the titanium tanning agent has a significant effect on the yield, morphology, and crystal phase of the product with other conditions unchanged. The concentrations of citric

Table 4 Ti contents of catalysts

Sample	Initial data from ICP-AES (mg/L)	Ti/wt%
0%Tb^{3+}–TiO_2	3.028	59.78
2% Tb^{3+}–TiO_2	2.989	60.56
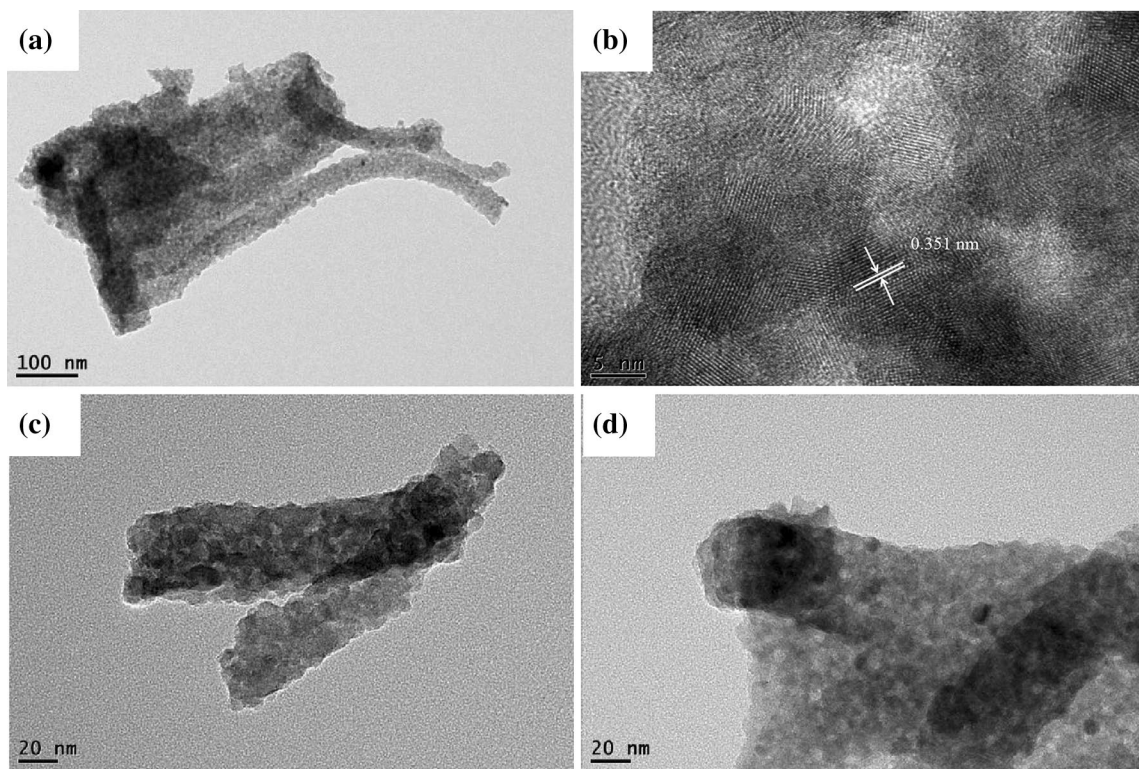
Fig. 7 TEM images of pure TiO$_2$ and 2% Tb^{3+}–TiO$_2$ calcined at 500 °C for 4 h. **a** Fibrous structure of Tb^{3+}-doped TiO$_2$; **b** polycrystalline structure of undoped TiO$_2$; **c** grains of undoped TiO$_2$,; **d** grains of Tb^{3+}-doped TiO$_2$
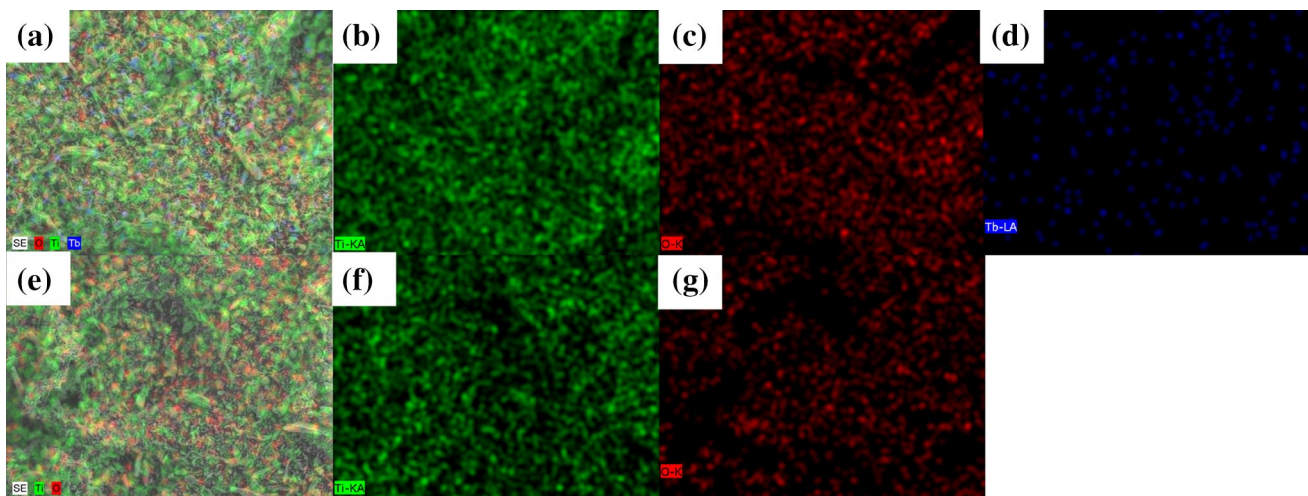
Fig. 8 Element mapping images of pure TiO$_2$ and 2% Tb^{3+}–TiO$_2$ calcined at 500 °C for 4 h. **a** Full image of element distribution in Tb^{3+}-doped sample; **b** Ti distribution in Tb^{3+}-doped sample; **c** O distribution in Tb^{3+}-doped sample; **d** Tb distribution in Tb^{3+}-doped sample; **e** full image of element distribution in undoped sample; **f** Ti distribution in undoped sample; **g** O distribution in undoped sample

acid and sodium citrate in the titanium tanning agent are changed using the following two methods.

1) *Method 1* 21.00 g solid citric acid and 0.05 g solid sodium citrate were dissolved in water to obtain a solution (1000 mL), from which 30 mL was taken to a beaker (50 mL).

2) *Method 2* 2.10 g solid sodium citrate was added into a 50 mL beaker, then just enough water is added to dissolve it, and the pH value was controlled to be 1–2.

Figure 9a, b are the SEM images of titanium dioxide prepared by Method 1 and 2, respectively. The calcination temperature to obtain mesoporous titanium dioxide is 600 °C, and other preparation conditions are kept the same. The TiO_2 synthesized using Method 1 (Fig. 9a) has an obvious fiber structure, while the sample prepared using Method 2 almost lost the fiber structure (Fig. 9b). The yields of titanium dioxide prepared using these two methods (Fig. 9a, b) differ significantly. The theoretical yield is 0.8 g when 2.4 g titanium sulfate is used as titanium source. Based on repeated verification experiments, the average yield of Method 1 can reached 79.67%, while that of Method 2 is only 13.67%.

These results show that the composition and concentration of titanium tanning agent have significant effects on the morphology and yield of titanium dioxide. In the tanning process, the role of tanning agent is to convert the raw hides into leather, and pH value plays a dominant role on the performance of leather. Therefore, the requirement for pH is quite strict in the preparation of titanium tanning agent. When too much citric acid is added, the performance of leather is not good, which affects the morphology and structure of titanium dioxide.

Figure 10 illustrates XRD patterns of titanium dioxide prepared using different concentrations of citric acid and sodium citrate in titanium tanning agent (a for Method 2 and b for Method 1). Both patterns a and b fit the peaks of anatase TiO_2, but the peak intensity of sample a is significantly weaker than that of sample b.

The above results show that the highest yield is obtained using Method 1 when the concentrations of citric acid and sodium citrate in the titanium tanning agent are changed.
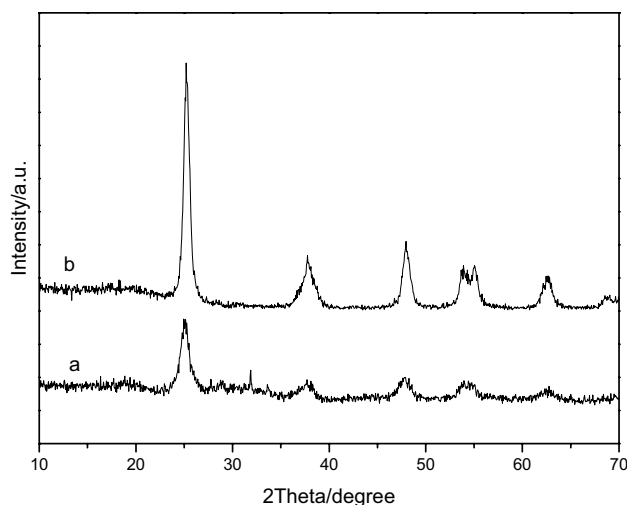
Fig. 10 XRD patterns of the TiO_2 prepared by different concentrations of citric acid and sodium citrate in titanium tanning agent

The intensity of the characteristic peak in the XRD pattern is stronger than that of the sample synthesized with the titanium tanning agent of high concentration, and the products also retain the fibrous structure of collagen template. In addition, the photocatalytic property of titanium dioxide prepared by Method 1 is much better than that of the sample prepared using Method 2. The reason is that the high concentration of titanium tanning agent and low pH value cause the over-tanning phenomenon during the process of initial tanning, which results in such outcomes such as a low yield.
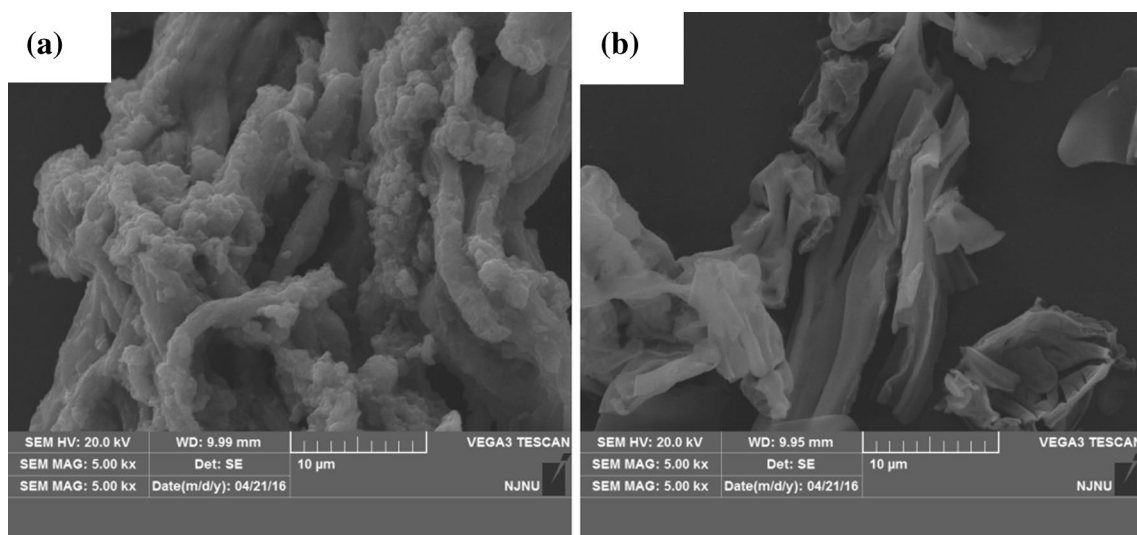
Fig. 9 SEM images of the samples prepared by different concentrations of titanium tanning agent. **a** Method 1, and **b** Method 2

4 Conclusions

The morphology, surface structure and crystalline phase of fibrous TiO$_2$ prepared using collagen as the template are different after doping with Tb^{3+}, and the effect of doping on the average grain size of the prepared titanium dioxide depends on the calcination temperature. The appropriate doping of Tb^{3+} can affect the lattice structure of TiO$_2$, and it can inhibit the recombination of photogenerated electrons and holes, which results in the increased photocatalytic performance of TiO$_2$. The degradation level of methyl orange by 2% Tb^{3+}–TiO$_2$ calcined at 500 °C for 4 h can reach 93.87% after photocatalytic degradation for 6 h. An excellent performance of titanium tanning, a high yield, and a fibrous structure of titanium dioxide can be presented when 0.2 mol/L citric acid/sodium citrate buffer solution is introduced.

References

1. Q. Luo, Q.Z. Cai, A novel method to synthesize molybdenum doped TiO$_2$ films with enhanced photocatalytic activity. Appl. Phys. A Mater. Sci. Process. **123**(6), 451 (2017)
2. X.S. Gao, Z.J. Tian, Z.D. Liu et al., Interface characteristics of Al$_2$O$_3$-13%TiO$_2$ ceramic coatings prepared by laster cladding. Trans. Nonferrous Met. Soc. China **22**(10), 2498–2503 (2012)
3. H.F. Chen, P.S. Tang, G.X. Pan et al., Preparation of Ag/TiO$_2$/PA self-cleaning paint by In-suit polymerization and its antimicrobial properties. Rare Metal Mater. Eng. **41**, 254–257 (2012)
4. D. Qian, R.J. Cheng, Z.G. Lu et al., TiO$_2$/SiO$_2$ core shell structured particles: assembly and electrochemical characteristics. Chin. J. Inorg. Chem. **23**(2), 305–309 (2007)
5. L. Ling, X.X. Wang, H. Wong et al., Modification of CoMo/TiO$_2$–Al$_2$O$_3$ catalyst by gas phase fluorination. Chin. J. Phys. Chem. **19**(1), 70–74 (2003)
6. W.D. Zhang, J.T. Li, P.Y. Gu et al., Temperature programmed decomposition of NO over Er$_2$O$_3$/Bi$_2$O$_3$ catalysts. Chin. J. Chem. **19**(6), 961–963 (1998)
7. H.L. Zheng, J.H. Zhang, W.Q. Xiong, New progress in the study on and application of organic pollutants photodegraded by Nano-TiO$_2$. Spectrosc. Spectr. Anal. **24**(8), 1003–1008 (2004)
8. J.X. Low, B. Chen, J.G. Yu, Surface modification and enhanced photocatalytic CO$_2$ reduction performance of TiO$_2$: a review. Appl. Surf. Sci. **392**, 658–686 (2017)
9. M.R. Hoffman, S.T. Martin, W. Choi et al., Environmental applications of semiconductor photocatalysis. Chem. Rev. **95**(1), 69–96 (1995)
10. W.K. Zhao, Y.L. Fang, K.C. Zhang et al., Preparation of nanosized anatase TiO$_2$ powder with high thermal stability. J. Inorg. Mater. **16**(4), 608–612 (1998)
11. X.H. Liu, X. Wang, X.J. Yang et al., Preparation, characterization and application of nanocrystalline titania. Jiangsu Chem. Ind. **27**(5), 5–7 (1999)
12. Z.Z. Yang, Ultrafine TiO$_2$—a new type of chemical material with broad prospect. Mod. Chem. Eng. (1), 38–40 (1994)
13. J.G. Zhou, X.S. Niu, The fine inorganic chemicals. (Higher Education Press, Beijing, 1999)
14. N. Lu, X. Quan, J. Li, S. Chen et al., Fabrication of boron-doped TiO$_2$ nanotube array electrode and investigation of its photoelectrochemical capability. J. Phys. Chem. C **111**(22), 11836–11842 (2007)
15. N. Masahashi, M. Oku, Superhydrophilicity and XPS study of boron-doped TiO$_2$. Appl. Surf. Sci. **254**(21), 7056–7060 (2008)
16. X.C. An, L.J. Han, Z.Y. Chen et al., Preparation of nitrogen doped TiO$_2$ powder by sol-gel method. Petrochem. Ind. **40**(9), 1000–1005 (2011)
17. Y.N. Zhao, G. Liu, C.H. Sun et al., Doping states of boron in nanocrystalline TiO$_2$ powder. J. Mater. Res. **22**(2), 125–129 (2008)
18. H.G. Li, J. Yan, S.G. Du et al., Investigation on the stability of W/O emulsion and microencapsulation of nano-TiO$_2$ sol. J. Adv. Chem. Eng. **28**(4), 858–863 (2014)
19. Y. Cheng, J.Q. Cheng, S. Ding, Controlled synthesis of nanosized TiO$_2$ powder using high-temperature vapor phase process. J. Chem. Eng. **58**(8), 2103–2109 (2007)
20. D.C. Li, D.L. Zhou, H. Liu et al., Preparation of nanometre TiO$_2$. Sichuan Nonferrous Met. (2), 1–8 (2003)
21. S. Islam, N. Bidin, S.S. Osman et al., Synthesis and characterization of Ni NPs-doped silica–titania nanocomposites: structural, optical and photocatalytic properties. Appl. Phys. A Mater. Sci. Process. **123**(1), 67 (2017)
22. X. Zhao, P. Liu, M. Wu et al., Y$_2$O$_3$ modified TiO$_2$ nanosheets enhance the photocatalytic removal of 4-chlorophenol and Cr(VI) in sunlight. Appl. Surf. Sci. **410**, 134–144 (2017)
23. T.H. Hou, Study on the structure and electronic properties of lanthanide-doped Nano-TiO$_2$. (Sichuan University, Chengdu, 2006)
24. X.H. Liu, Z.C. Wu, Y.W. Zhao et al., Effects of doping micro platinum on the structures and performances of TiO$_2$ powder. J. Chem. **67**(6), 507–512 (2009)
25. X.H. Liu, X.B. He, Y.B. Fu, Effects of doping cobalt on the structures and performances of TiO$_2$ photocatalyst. J. Chem. **66**(14), 1725–1730 (2008)
26. W. Yang, H. Guo, W.H. Zhang et al., Preparation and catalytic activity for degradation of acidic fuchsine of TiO$_2$ photocatalyst. Spectrosc. Spectr. Anal. **28**(4), 922–925 (2008)
27. W.L. Liu, H.B. Zhang, J.H. Chen et al., The preparation and properties of Nitrogen-doped TiO$_2$ photocatalyst. Rare Met. Mater. Eng. **36**(S2), 430–433 (2007)
28. X.Y. Zhang, X.L. Cui, Preparation and photocatalytic hydrogen evolution performance of C-N Co-doped Nano TiO$_2$ photocatalysts. Chin. J. Phys. Chem. **25**(9), 1829–1834 (2009)
29. T.S. Jiang, L. Zhang, M.R. Ji et al., Carbon nanotubes/TiO$_2$ nanotubes composite photocatalysts for efficient degradation of methyl orange dye. Particuology **11**(6), 737–742 (2013)
30. Y. Shiraishi, A. Naoya Saito, T. Hirai, Adsorption-driven photocatalytic activity of mesoporous titanium dioxide. J. Am. Chem. Soc. **127**(37), 12820 (2005)
31. J.G. Yu, Y.R. Su, B. Cheng, Template-free fabrication and enhanced photocatalytic activity of hierarchical macro-mesoporous titania. Adv. Funct. Mater. **17**(12), 1984–1990 (2007)
32. J.X. Zhao, Research progress of the template method used for TiO$_2$ photocatalyst. Shanghai Chem. **36**(10), 22–25 (2011)
33. L. Liu, Y. Hu, W.H. Dan et al., Molecular mechanism in process of fiber opening-up. China Leather **42**(3), 10–12 (2013)
34. D.H. Deng, R. Tang, X.P. Liao et al., Using collagen fiber as a template to synthesize hierarchical mesoporous alumina fiber, Langmuir: the ACS. J. Surf. Colloids **24**(2), 368–370 (2008)

35. N.N. Yan, Y. Zhang, J. Wu et al., Research progress on TiO_2 photocatalyst doped with RE Ions. Mater Herald **25**(17), 72–74 (2011)

36. B. Choudhury, B. Borah, A. Choudhury, Ce-Nd codoping effect on the structural and optical properties of TiO_2 nanoparticles. Mater. Sci. Eng. B **178**(4), 239–247 (2013)

37. Z.W. Zhang, J. Fan, Effect of doping Tb on photocatalytic activity of Nano-TiO_2. Petrochem. Ind. **36**(9), 956–960 (2007)

38. Q. Lan, Preparation and photocatalytic activity study of nonmetal and lanthanum Co-doped titanium dioxide catalyst. Shanghai: East China University of Science and Technology, (2013)

39. X.H. Wu, L.S. Shi, W. Qin et al., Titanium dioxide films grown on Ti substitute and their photo-catalytic activities. J. Harbin Inst. Technol. **38**(11), 1919–1922 (2006)

40. X. Wang, R.G. Li, Q. Xu et al., Roles of (001) and (101) facets of anatase TiO_2 in photocatalytic reactions. Chin. J. Phys. Chem. **29**(7), 1566–1571 (2013)

41. H.X. Zhang, Y.H. Zhang, Y.X. Xu et al., Phase transition and photocatalytic properties of terbium doped nanosized titanium dioxide. J. Chem. **61**(11), 1813–1818 (2003)

42. J. Lin, C.Y. Jimmy, An investigation on photocatalytic activities of mixed TiO_2 rare earth oxides for the oxidation of acetone in air. J. Photochem. Photobiol. A Chem. **116**(1), 63–67 (1998)

43. X.Y. Yu, J.J. Chen, Y.J. Du, An investigation on phase transformation and photocatalytic activities of mixed TiO_2-rare earth oxidation. Glass Enamel **28**(2), 15–20 (2000)

44. A.W. Xu, Y. Gao, H.Q. Liu, The preparation, characterization, and their photocatalytic activities of rare-earth-doped TiO_2 nanoparticles. J. Catal. **207**(2), 151–157 (2002)

45. L.Y. Zhang, Z.X. Liu, X.L. Yu et al., Preparation and photocatalytic property of Ag-doped TiO_2. J. Funct. Mater. **41**(12), 2169–2173 (2010)

46. S.W. Deng, J. Yu, C. Yang et al., Gd, I-doped TiO_2 thin films coated on solid waste material: synthesis, characterization, and photocatalytic activity under UV or visible light irradiation. Appl. Phys. A Mater. Sci. Process. **123**, 639 (2017)

47. S. Paul, B. Choudhury, A. Choudhury, Magnetic property study of Gd doped TiO_2 nanoparticles. J. Alloy. Compd. **601**(27), 201–206 (2014)

48. G.L. Li, L. Li, K. Fu et al., Effect of active metal yttrium film on oxygen concentration in terbium. J. Funct. Mater. **46**(23), 23061–23063 (2015)

49. V. Kumar, O.M. Ntwaeaborwa, J. Holsa et al., The role of oxygen and titanium related defects on the emission of TiO_2:Tb^{3+} nanophosphor for blue lighting applications. Opt. Mater. **46**, 510–516 (2015)

50. Y.Y. Zhang, D. Gu, L.Y. Zhu et al., Highly ordered Fe^{3+}/TiO_2 nanotube arrays for efficient photocatalytic degradation of nitrobenzene. Appl. Surf. Sci. **420**, 896–904 (2017)